SUPPLEMENTARY

Optimising Electron-Rich 2D Fe,B-$Ti_3C_2T_x$/ N-doped mixed metal oxide Interface for Industrial-Scale Oxygen Evolution in Seawater

Sharafadeen Gbadamasi [1], Takaya Fujisaki [2], Suraj Loomba [1], Karishma Jain [3,4,5], Muhammad Tayyab Shuja [3], Seyedmahdi Mousavi [1], Vasundhara Nettem [3], Muhammad Waqas Khan [1,3], Muhammad Haris [1], Lars Thomsen [6], Anton Tadich [6], Jian Xian [7], Nasir Mahmood [1,3,*]

[1]School of Engineering, RMIT University, Melbourne, Victoria, 3000, Australia

[2]Faculty of Materials for Energy, Shimane University, Matsue, Shimane, 690-8504, Japan

[3]School of Science, RMIT University, Melbourne, Victoria, 3000, Australia

[4]Advanced Carbon Products and Metrology Department, CSIR-National Physical Laboratory (CSIR-NPL), New Delhi, 110012, India

[5]Academy of Science and Innovation Research, Ghaziabad, 201002, India

[6]Australian Synchrotron, ANSTO, 800 Blackburn Road, Clayton, Victoria, 3168, Australia

[7]School of Materials and Energy, University of Electronic Science and Technology of China, Chengdu 611731, China

*Corresponding Author: Nasir Mahmood (Email: nasir.mahmood@rmit.edu.au)

Experimental Methods

Materials

Iron(III) nitrate nonahydrate ($Fe(NO_3)_3.9H_2O$), ≥98% (Sigma); Boric acid ($B(OH)_3$) ≥99.5% (Sigma); Ti_3AlC_2 powder (Sigma); HF solution (48 wt. % in H_2O, ≥99.99% trace metals basis) (Sigma); Sodium hydroxide (NaOH), ≥98% (Sigma); potassium hydroxide (KOH), ≥85% (Sigma); Diethyl-p-phenylene diamine (DPD), 97% (Sigma); Absolute methanol (Sigma); Polytetrafluoroethylene (PTFE) (Sigma); Isopropyl alcohol (Sigma); Hydrochloric acid (Sigma); Absolute ethanol (Sigma); Hexamethylenetetramine (HMTA), ≥99%; Mo powder, 99.9% (Sigma); Hydrogen peroxide (Sigma); Ni foam; Seawater (sourced from Altona Beach, Melbourne, Australia)

Synthesis of Materials

Synthesis of $Ti_3C_2T_x$ MXene: $Ti_3C_2T_x$ MXene was synthesized following the methodology established by Yuri and colleagues, albeit with certain modifications [1]. In summary, 2 g of Ti_3AlC_2 powder was incrementally introduced into 40 ml of a 10% HF solution, and the mixture was stirred at 500 rpm and 35 °C for 24 hours in a water bath. The resulting product was distributed into three 50 ml centrifuge tubes, each containing approximately 25 ml of milli-Q water. These tubes were subsequently sealed and centrifuged at 5000 rpm for 5 minutes. The supernatant was discarded, and additional milli-Q water was added to the sediment for further washing, with this process being repeated until a pH of approximately 7 was achieved. To ensure the complete removal of fluoride ions, the neutral sediment (wet $Ti_3C_2T_x$) was dispersed in 1 l of milli-Q water, and the solid was recovered through vacuum filtration utilizing a 0.2-micron PES filter membrane. Following filtration, the product was vacuum dried at 50 °C overnight.

$Ti_3C_2T_x$ surface modification using 0.1 M NaOH: 2g of dried $Ti_3C_2T_x$ were subjected to treatment with 20 ml of 0.1 M NaOH solution while stirring at room temperature for 24 hours. The resulting solid product was isolated through centrifugation and underwent several washings with deionized water until achieving a pH of approximately 7. The neutral solid was then redispersed in deionized water and sonicated for 15 minutes. The solid product was subsequently collected via vacuum filtration, dried overnight under vacuum at 50 ^oC, and designated as $Ti_3C_2O_2$.

Material Characterizations

The X-ray diffraction (XRD) patterns were recorded utilizing a Bruker D4 Endeavor analyser, employing Cu Kα radiation at operational settings of 35 mA and 40 kV. Morphological imaging, selected area electron diffraction (SAED) analysis, and energy-dispersive X-ray spectroscopy (EDX) were conducted using transmission electron microscopes (JEOL-2100F). The surface chemistry of the material was analysed using a high-resolution X-ray photoelectron spectrometer (XPS) from Thermo Scientific, which was equipped with an Al Kα monochromatic X-ray source. Scanning was executed with a dwell time of 50 ms^{-1} per point and a pass energy of 50 eV. Near-edge X-ray absorption fine structure (NEXAFS) data were collected at the high-throughput NEXAFS endstation located at the soft X-ray beamline of the Australian synchrotron. The spectra were recorded in Partial Electron Yield (PEY) mode, utilizing a retarding grid-based channeltron detector, which was adjusted to the appropriate bias for each element to capture the relevant Auger electrons. All spectra were normalized to the incident photon flux, employing a transmissive gold mesh positioned before the sample and analysed using the QANT program [2, 3].

OER selectivity evaluation

To measure the Faradaic efficiency, amperometry (i-t) curve technique was employed using 6 M alkaline seawater electrolyte, 1.9 V vs RHE, and the gas generated was collected and measured over water [4]. The detailed calculation is presented in Faraday's efficiency calculation of this supplementary information. Further, the presence of ClO^- was evaluated by testing amperometry (i-t) curve stability in 6 M alkaline seawater electrolyte at 1.9 V vs RHE for 24 hours. Thereafter, the electrolyte was collected and tested for the presence of ClO^- using the diethyl-p-phenylene diamine (DPD) method. Firstly, the pH of the collected electrolytes and filtered natural seawater was adjusted to ~7.1 followed by the addition of the DPD reagent. The mixture was agitated and allowed to stay for around 3-5 minutes to observe any colour change.

$$Faraday's\ efficiency\ (FE)\ (\%) = \frac{Moles\ of\ O_2\ detected\ (experimental)(n_{exp})}{Moles\ of\ theoretical\ oxygen\ (n_{theory})} \times 100$$

Computational methods

Structure

All density functional theory (DFT) calculations were performed using the Vienna Ab initio Simulation Package (VASP, version 6.4.3), except where stated otherwise [5-9]. The Perdew–Burke–Ernzerhof parametrization under the generalized gradient approximation (GGA) was employed as the exchange-correlation functional, in combination with the projector-augmented wave (PAW) method [6]. A plane-wave cutoff energy of 500 eV was chosen to balance computational cost and convergence following previous study [10]. The crystal model of FBT and that of NMO were constructed for geometry optimization, ensuring that their compositions closely matched experimentally data. As for NMO, it has three oxygen vacancy sites, and their locations are shown in **Fig.** S1. The crystal structures of both FBT and NMO were combined to create a stable interface optimized by VASP. The optimizations were performed using the conjugate gradient method until

the residual forces acting on each atom were less than 10^{-2} eV/Å, and the electronic energy was converged to within 10^{-7} eV. The Monkhorst-Pack method was used to sample the k-point mesh with a 1 × 1 × 1 grid for the interface structure. Also, to determine the local charge of atoms in the system, bader analysis was employed [11-14]. Spin polarization was considered for all calculations. Ionic cores of all atoms were described using projector augmented wave (PAW) pseudopotentials from the VASP library (PAW_PBE B, C, N, O, Cl, H, Ti_sv, Fe_pv, Mo_pv, and Ni_pv) following previous studies [15-17].

OER Mechanism

We evaluated the oxygen-evolution reaction (OER) energies on the MNO surface, the FBT surface, and the FBT-NMO interface by means of a deep-learning potential implemented in Matlantis. The PreFerred Potential (PFP) model version 8.0 built into Matlantis, developed by Takamoto *et al.*, is a universal neural-network potential (NNP) that reproduces density-functional-theory (DFT) accuracy while running roughly 10^4 times faster[18, 19]. Previous studies have shown that Matlantis/PFP agrees well with conventional PBE+U DFT in calculating surface energies of metal (oxy)hydroxides and oxides[20]. Because conventional DFT becomes prohibitively expensive for systems exceeding ~500 atoms, we exploited Matlantis to handle more large-scale interface model that would otherwise be extremely difficult to treat.

As initial geometries we prepared the most stable surfaces of the FBT model and the NMO model together with a slab in which the two were joined to form the FBT-NMO interface. All of these structures had been pre-optimized by DFT (PBE + PAW) as shown in previous. The Matlantis calculations were carried out through a Python script based on the Atomic Simulation Environment (ASE). Atomic positions were relaxed with the BFGS algorithm until the residual force on every atom fell below 0.01 eV $Å^{-1}$. Spin polarization was included, and ferromagnetic initial spins were

assigned to the transition-metal atoms. Also, the PFP mode PBE+U+D3 was selected. In this mode, fixed Hubbard-U values and Becke–Johnson-damped DFT-D3 dispersion corrections are already built into the potential[21].

The OER proceeds through four proton-coupled electron-transfer (PCET) steps:

- Step1: $H_2O + * \rightarrow *OH + (H^+ + e^-)$, $\Delta G_1 = G(*OH) - G(*) - G(H_2O) + \frac{1}{2} G(H_2)$
- Step2: $*OH \rightarrow *O + (H^+ + e^-)$, $\Delta G_2 = G(*O) - G(*OH) + \frac{1}{2} G(H_2)$
- Step3: $H_2O + *O \rightarrow *OOH + (H^+ + e^-)$, $\Delta G_3 = G(*OOH) - G(*O) - G(H_2O) + \frac{1}{2} G(H_2)$
- Step4: $*OOH \rightarrow * + O_2 + (H^+ + e^-)$, $\Delta G_4 = G(*) - G(*OOH) + G(O_2) + \frac{1}{2} G(H_2)$

Here * denotes an active site on the catalyst surface, which indicates that there are no adsorbates. The reaction free-energy change ΔG for each step was obtained from total energies of the adsorbed species. For example, $\Delta G_1 = G(OH) - G(*) - G(H_2O) + \frac{1}{2} G(H_2)$. Analogous expressions were used for ΔG_2, ΔG_3 and ΔG_4. The reference energies $G(H_2O)$, $G(H_2)$ and $G(O_2)$ were taken from single molecule in vacuum state. Using these definitions, we calculated the energies of the adsorbed intermediates (*OH, *O, *OOH) on each surface and derived ΔG for all four steps.

OER over CER study

Furthermore, the stability of Cl within the interface was then evaluated (using DFT) using the insertion energy E_{ins} defined by Equation (S1):

$$E_{ins} = \frac{E_{host} + n \cdot E_{guest} - E_{guest+host}}{n} \quad \text{(S1)}$$

where E_{host} is the total energy of the system without inserted atom, E_{guest} is energy per atom of the inserted species in its reference state, $E_{guest+host}$ is the system's total energy with the guest atoms inserted, and n is the number of inserted atoms [22]. When the value of E_{ins} in the above equation

(S1) is positive, it indicates that the target substance is stabilized; a negative value, on the other hand, suggests destabilization.

Results

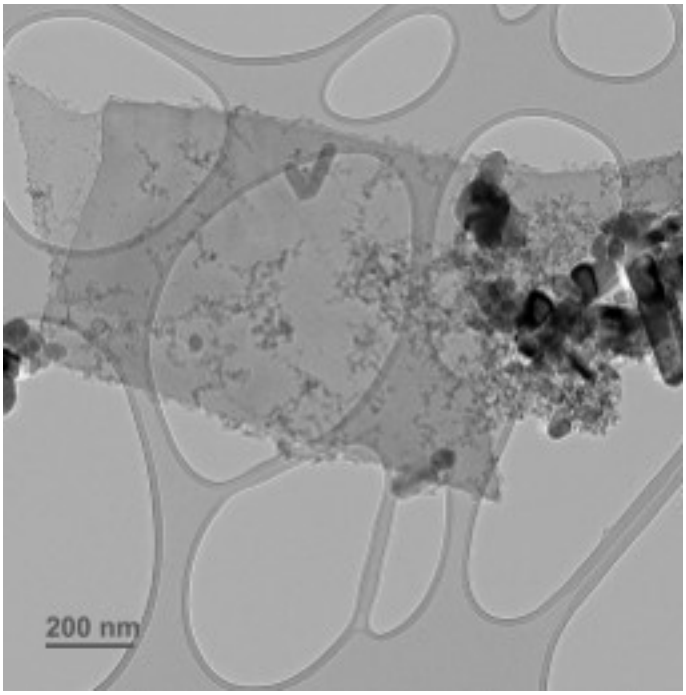

Fig. S1 TEM image of FBT.

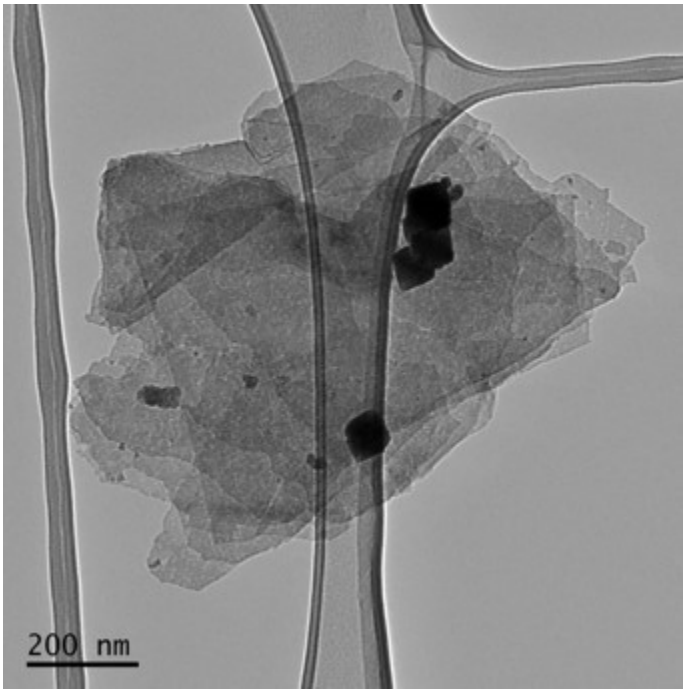

Fig. S2 TEM image of NMO.

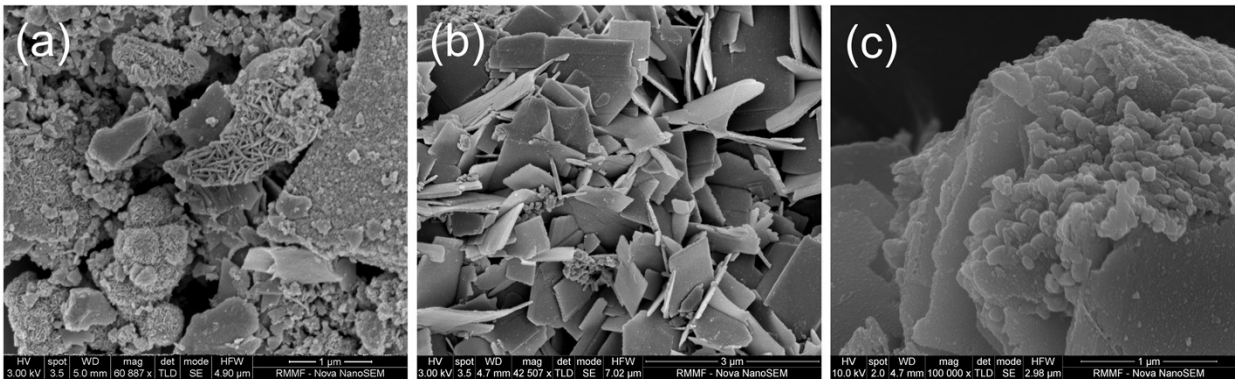

Fig. S3 SEM images of (a) NMO, (b) FBT, and (c) FBT/NMO(50)

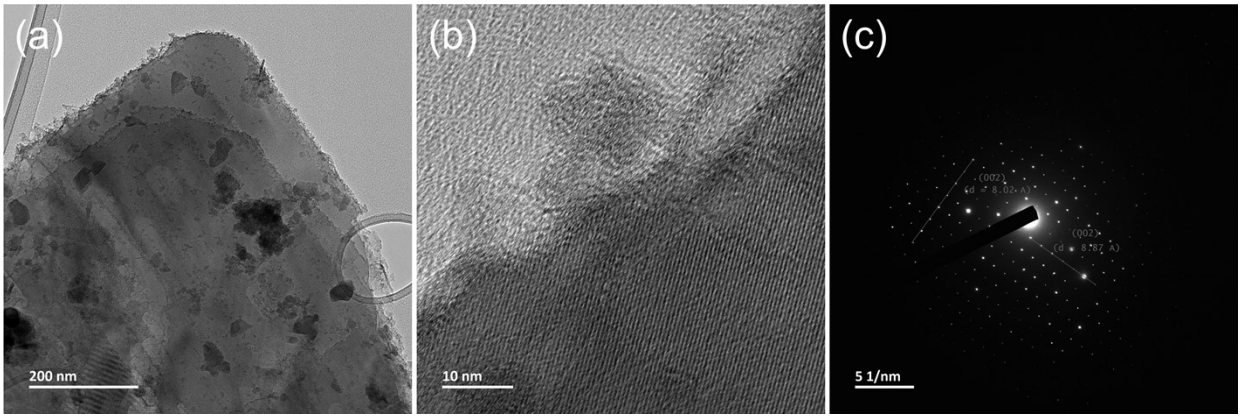

Fig. S4 (a) TEM, (b) HRTEM, and (c) SAED images of FBT/NMO(25).

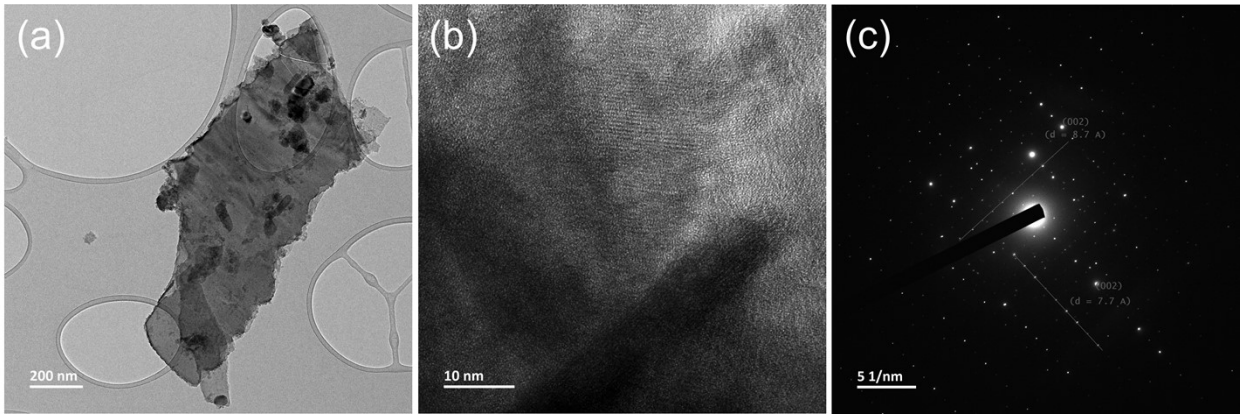

Fig. S5 (a) TEM, (b) HRTEM, and (c) SAED images of FBT/NMO(75).

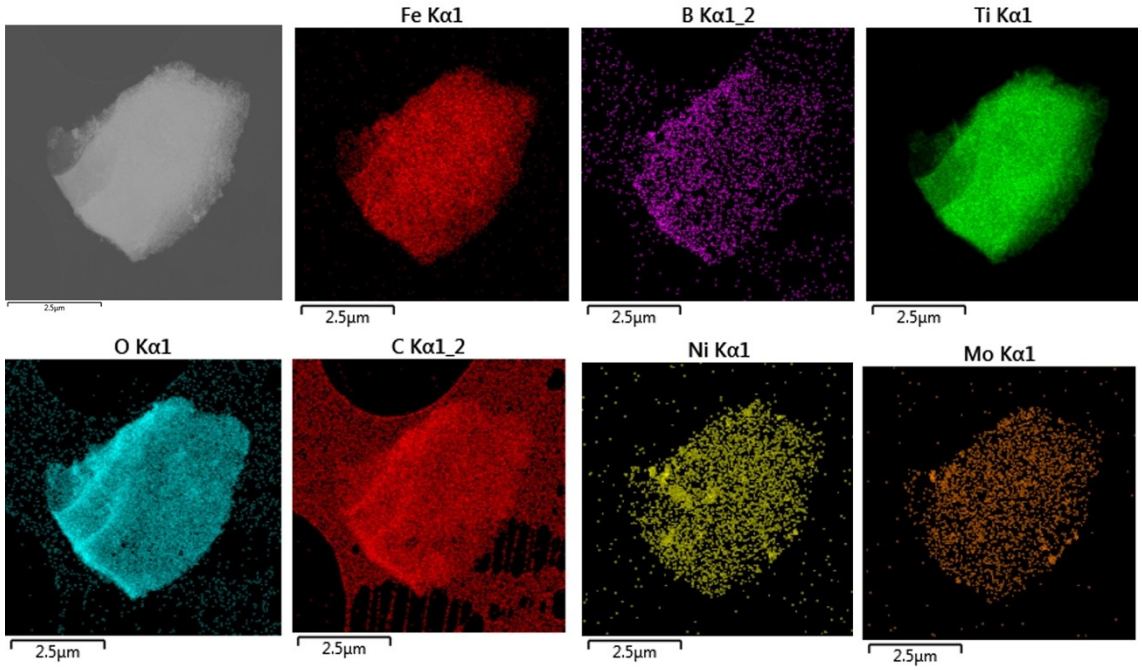

Fig. S6 EDX of FBT/NMO(25).

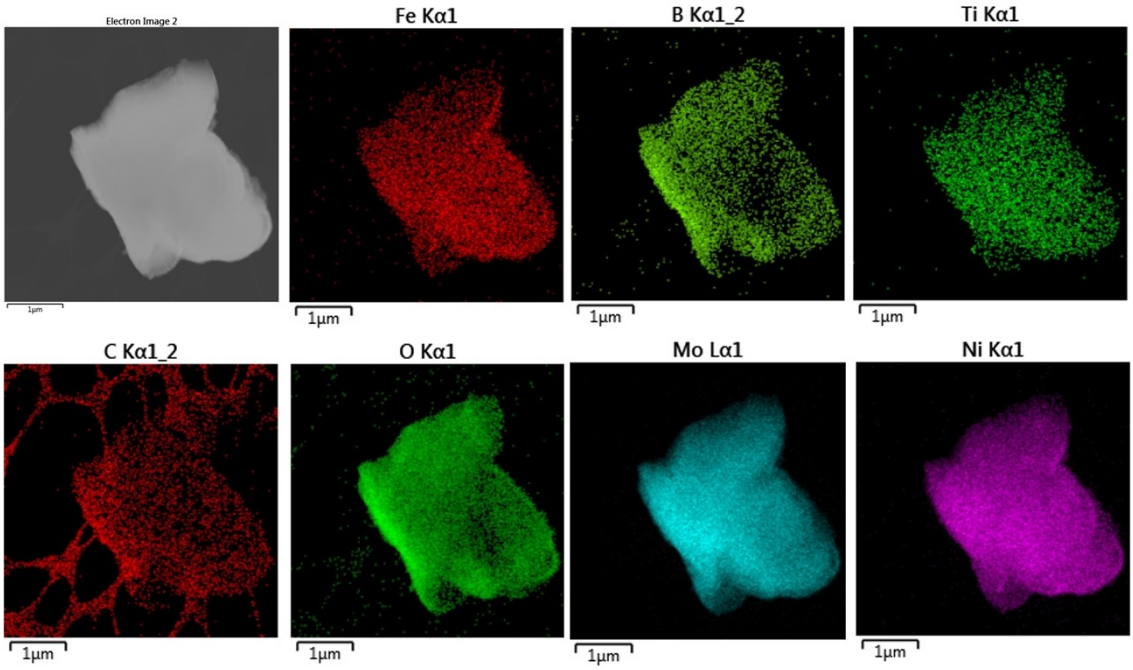

Fig. S7 EDX of FBT/NMO(75).

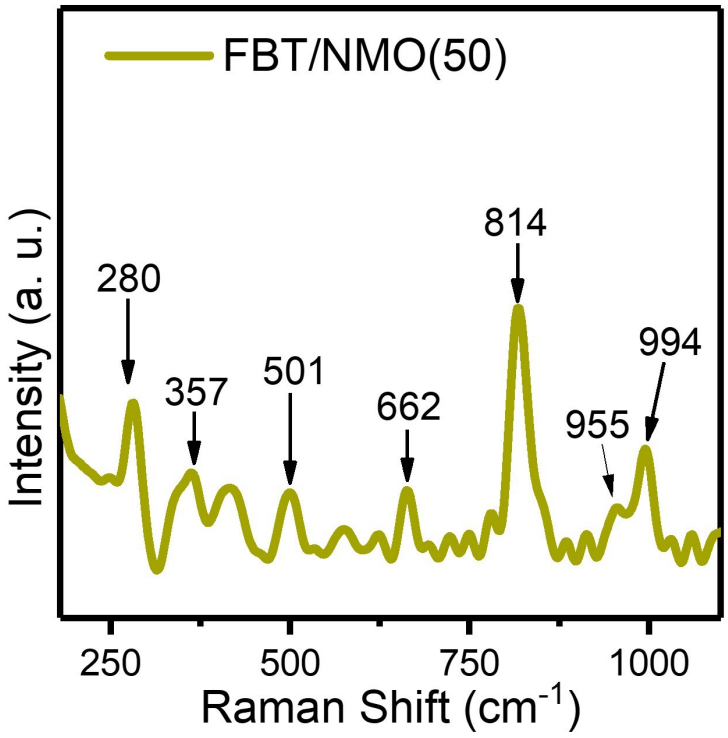

Fig. S8 Raman spectra of FBT/NMO(50) before and after OER.

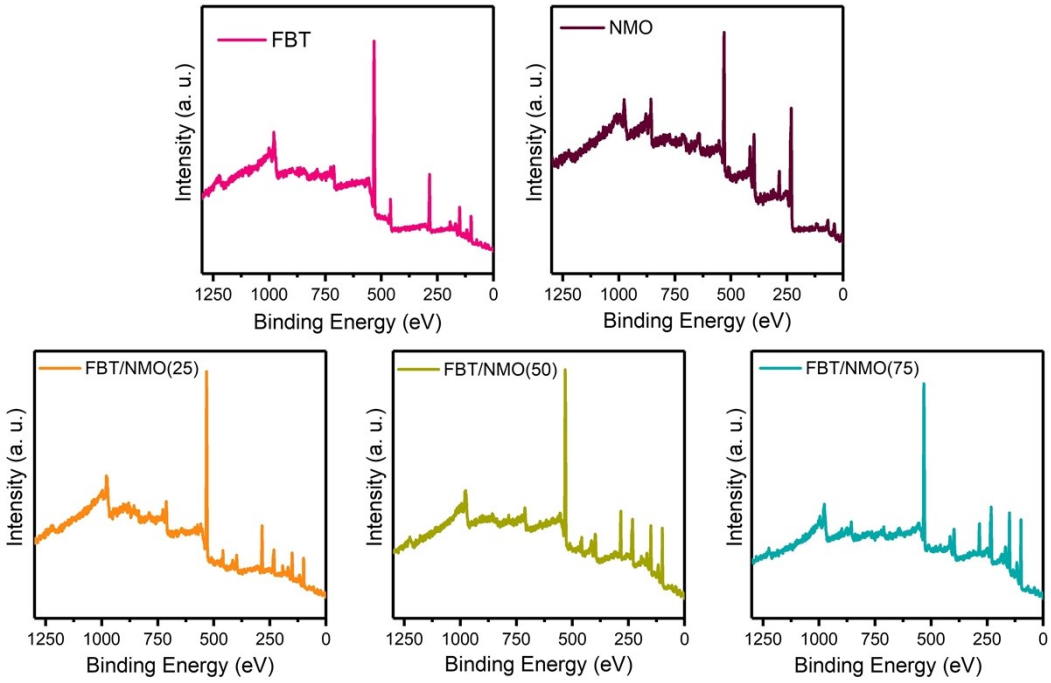

Fig. S9 XPS survey scans of FBT, NMO, FBT/NMO(25), FBT/NMO(50), and FBT/NMO(75).

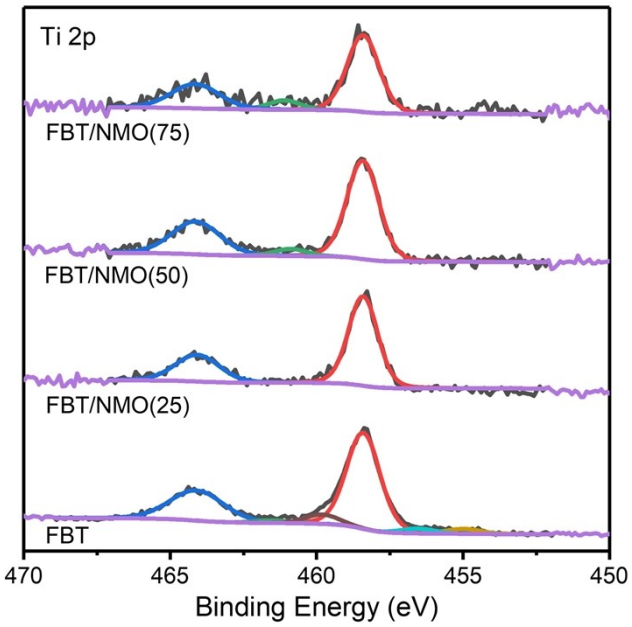

Fig. S10 Ti 2p fitted high-resolution XPS spectra of FBT, FBT/NMO(25), FBT/NMO(50) and FBT/NMO(75).

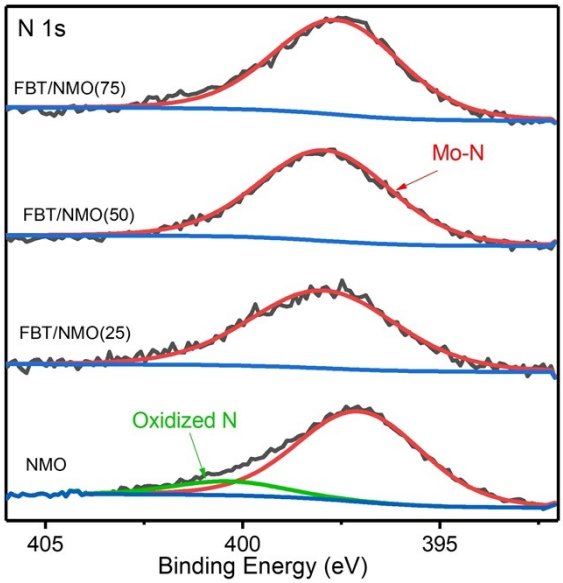

Fig. S11 Fitted N 1s high-resolution XPS spectra of NMO, FBT/NMO(25), FBT/NMO(50) and FBT/NMO(75).

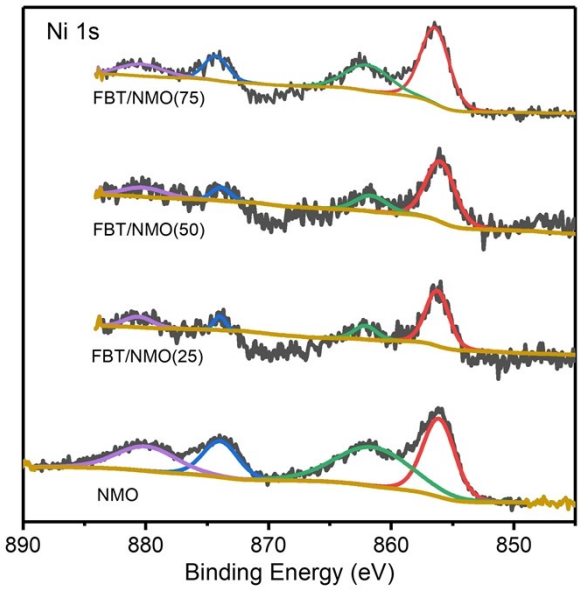

Fig. S12 Fitted Ni 1s high-resolution XPS spectra of NMO, FBT/NMO(25), FBT/NMO(50) and FBT/NMO(75).

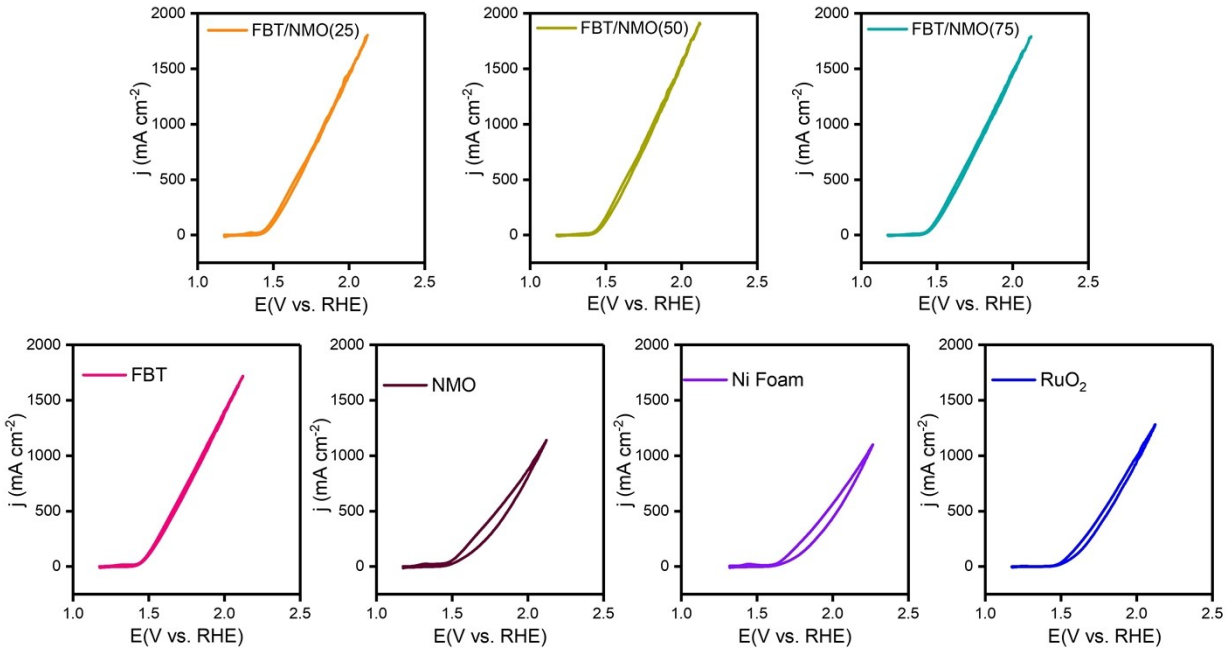

Fig. S13 Polarization curves showing both the forward and backward-sweep scans (CV) of FBT/NMO(25), FBT/NMO(50), FBT/NMO(75), FBT, NMO, Ni Foam, and RuO_2 at a scan rate of 5 mV s^{-1}.

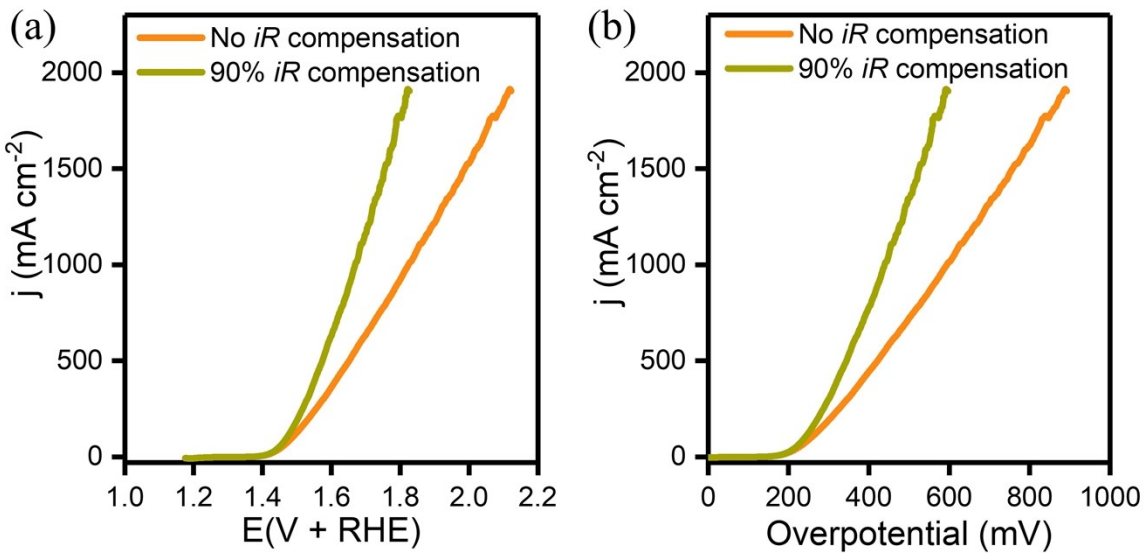

Fig. S14 Comparing the OER polarization curves of FBT/NMO(50) with and without *iR* compensation.

Table S1. A comparative analysis of the FBT/NMO(50) activity with some highly active catalysts evaluated with 90% iR compensation reported in the literature. The parameters η100 and η500 denote the overpotential necessary to achieve current densities of 100 and 500 mA cm^{-2}, respectively.

Catalyst	Electrolyte	Overpotential (mV)		Stability		Ref.
		η_{100}	η_{500}	j (mA cm^{-2})	Time (h)	
FBT/NMO(50)	6 M KOH + Seawater	240	344	~1500	>1000	This work
NiFe-CuCo LDH	6 M KOH + Seawater	259	283	500	500	[23]
CoFe-Ni_2P	6 M KOH + Seawater	266	304	500	600	[24]
NiCoFe LDH	6 M KOH + Seawater	~280	~440	10	12	[25]
	6 M KOH + 2 M NaCl	~280	~430			
	6 M KOH + Freshwater	~270	~440			
borate-intercalated nickel–cobalt–iron oxyhydroxides	10 M KOH + artificial seawater + Fe(II) ions	247	267	500	100	[26]
$Fe_{0.01}Ni\&Ni_{0.2}Mo_{0.8}N$	6 M KOH + Seawater	234	272	<450	80	[27]

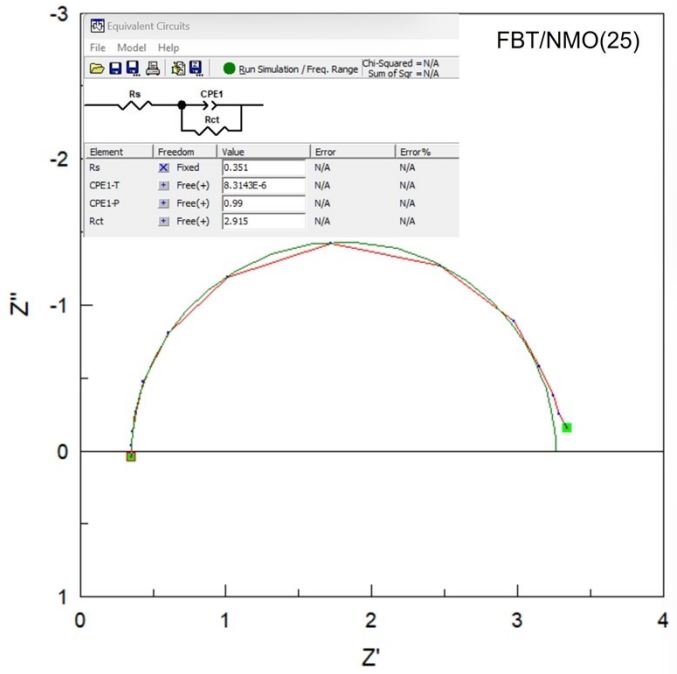

Fig. S15 Fitted Nyquist plot of FBT/NMO(25).

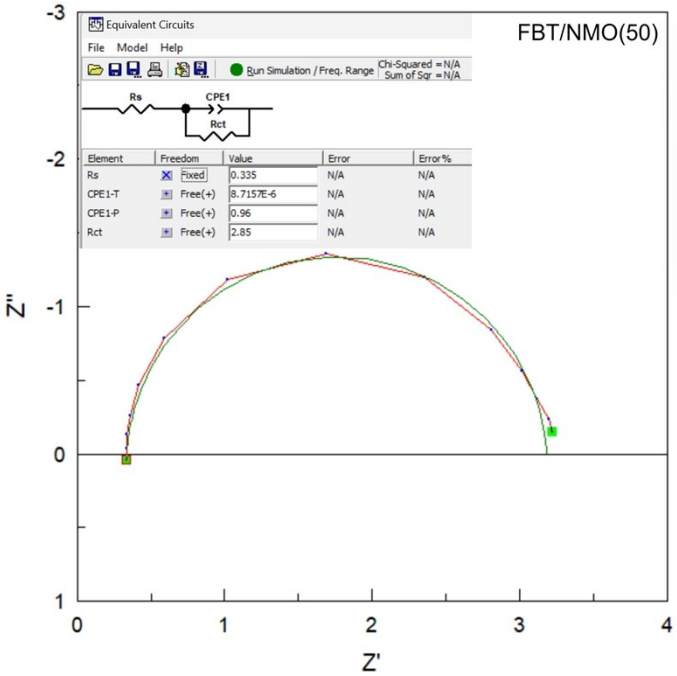

Fig. S16 Fitted Nyquist plot of FBT/NMO(50).

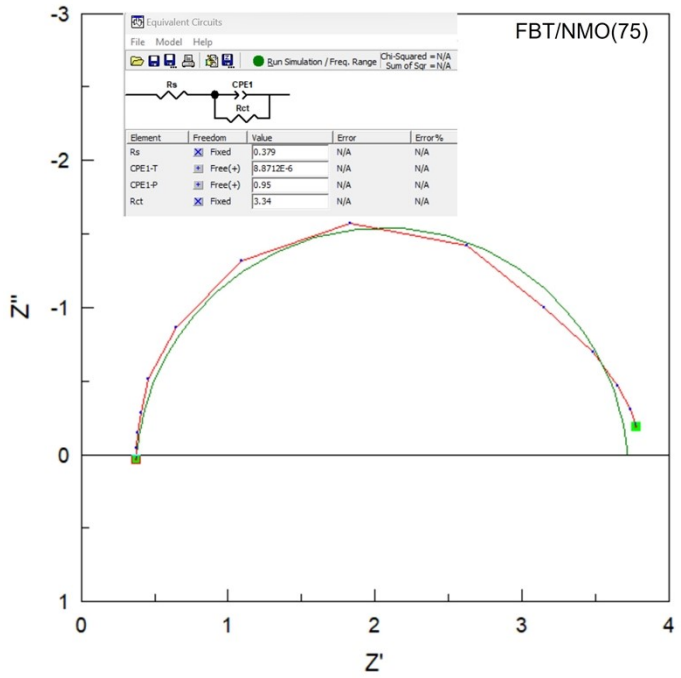

Fig. S17 Fitted Nyquist plot of FBT/NMO(75).

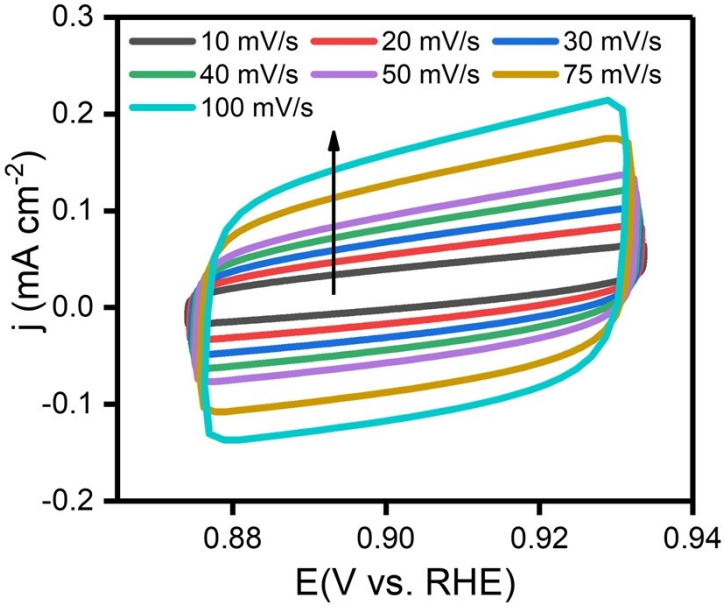

Fig. S18 Cyclic voltammetry (CV) curves of FBT/NMO(25) measured at different scan rates ranging from 10 to 100 mV s^{-1}.

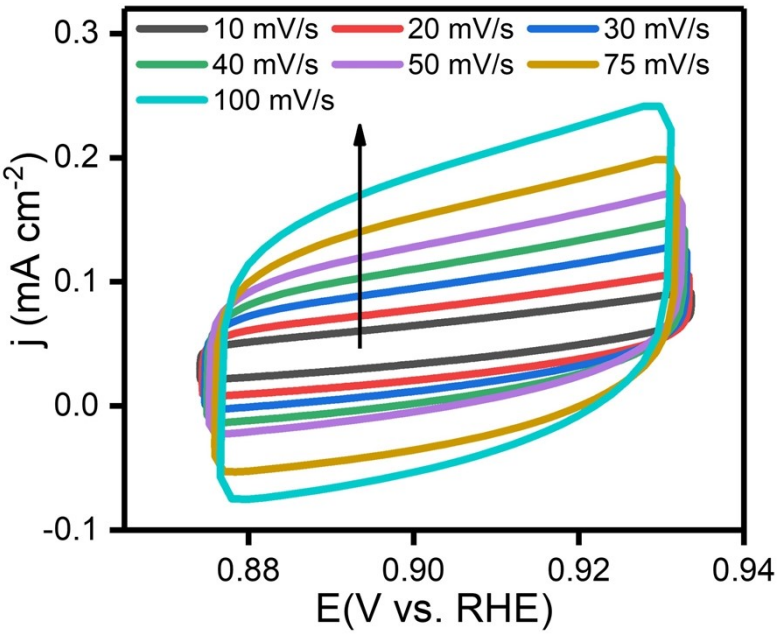

Fig. S19 Cyclic voltammetry (CV) curves of FBT/NMO(50) measured at different scan rates ranging from 10 to 100 mV s^{-1}.

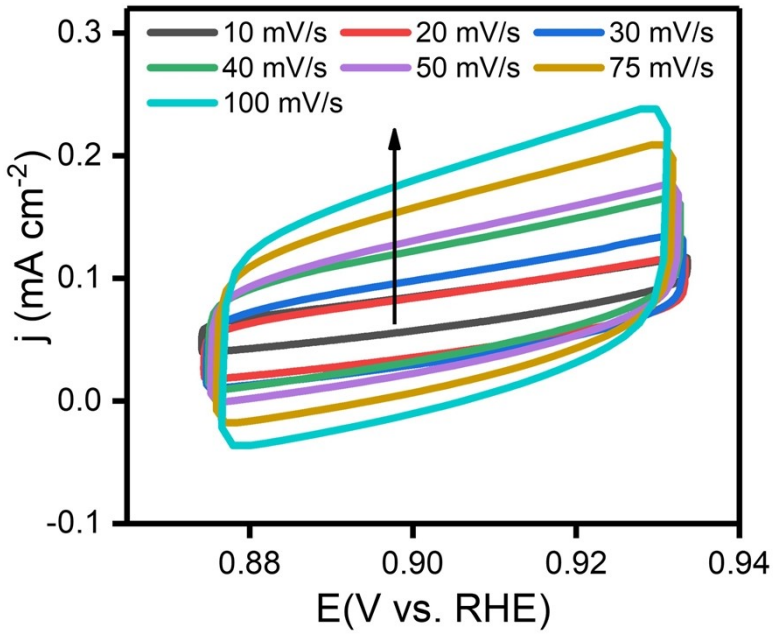

Fig. S20 Cyclic voltammetry (CV) curves of FBT/NMO(75) measured at different scan rates ranging from 10 to 100 mV s^{-1}.

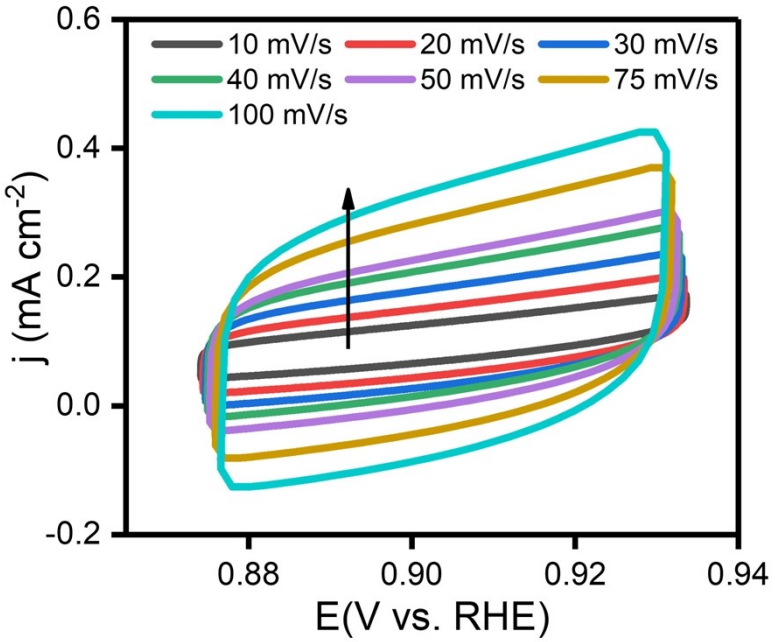

Fig. S21 Cyclic voltammetry (CV) curves of FBT measured at different scan rates ranging from 10 to 100 mV s^{-1}.

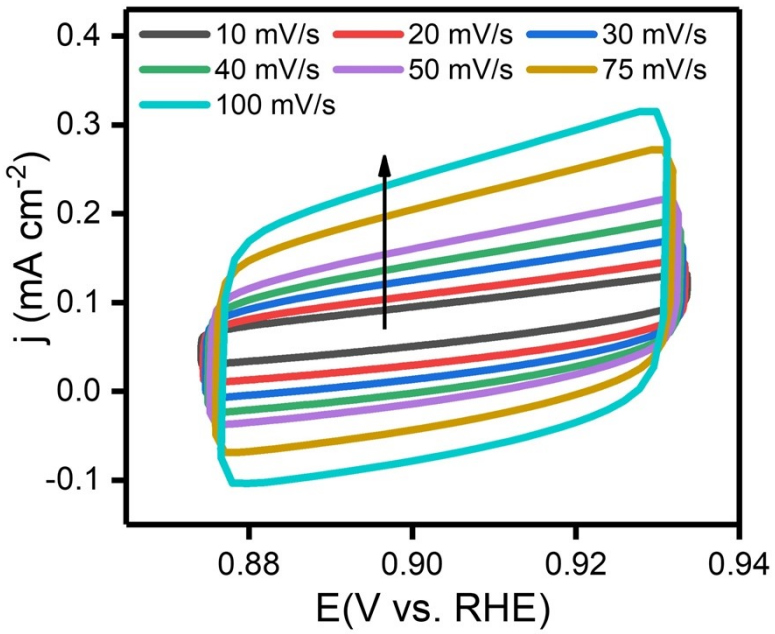

Fig. S22 Cyclic voltammetry (CV) curves of NMO measured at different scan rates ranging from 10 to 100 mV s^{-1}.

Calculation of electrochemical surface areas (ECSA)

The ECSA of FBT, NMO, FBT/NMO(25), FBT/NMO(50) and FBT/NMO(75) were calculated by using the equation:

$$ECSA = Geometric\ surface\ area \times \frac{C_{dl}}{C_s}$$

Where:

Geometric surface area is the surface area of the electrode used = 0.25 cm^2

C_{dl} is the experimentally calculated double layer capacitance (**Fig.** 3e) from CV curves in **Fig.** S12 - 16 (mF cm^{-2})

C_s is the capacitance of the flat electrode surface (Cs = 0.04 mF cm^{-2}) [24, 28].

$$ECSA_{FBT} = 0.25 \times \frac{3.96}{0.04} = 24.75\ cm^2$$

$$ECSA_{NMO} = 0.25 \times \frac{3.13}{0.04} = 19.5625\ cm^2$$

$$ECSA_{FBT/NMO(25)} = 0.25 \times \frac{2.65}{0.04} = 16.5625\ cm^2$$

$$ECSA_{FBT/NMO(50)} = 0.25 \times \frac{2.33}{0.04} = 14.5625\ cm^2$$

$$ECSA_{FBT/NMO(75)} = 0.25 \times \frac{1.84}{0.04} = 11.5\ cm^2$$

$$j_{ECSA} = \frac{Current\ Density}{ECSA}$$

Faraday's Efficiency (FE) Calculations

$$FE\ (\%) = \frac{Moles\ of\ O_2\ detected\ (experimental)(n_{exp})}{Moles\ of\ theoretical\ oxygen\ (n_{theory})} \times 100$$

To calculate moles of theoretical oxygen

$$n_{theory} = \frac{Total\ charge\ (Q)}{zF}$$

Where:

$$Total\ charge\ (Q) = Current\ (I)\ in\ Ampere\ \times\ Time\ (t)\ in\ seconds$$

F = Faraday's constant =~96500 C mol^{-1}

The oxidation of water to oxygen ($2H_2O \rightarrow O_2 + 4H^+ + 4e^-$) requires 4 moles of electrons to produce 1 mole of O_2. Therefore, z = 4

NB: The produced oxygen gas was collected over water at a 1.9 V vs RHE and the volume collected was measured at a fixed time of 8 mins.

$$t = 8\ mins = 8\ \times 60 = 480\ secs$$

Therefore,

$$n_{theory} = \frac{It}{zF} = \frac{I\ \times 480}{4\ \times 96500} = \frac{480I}{386000} = 0.0012435I\ mol$$

To calculate moles of experimental oxygen

From Dalton's law of partial pressure

$P_{total} = P_{water} + P_{oxygen}$

Where:

P_{total} is total pressure inside the measuring cylinder

P_{water} is vapour pressure of water

P_{oxygen} partial pressure of the produced oxygen

Laboratory Temperature = ~17 ^{o}C

From vapour pressure table, P_{water} = 14.53 mmHg

P_{total} = 762 mmHg

From

$P_{oxygen} = P_{total} - P_{water}$

$P_{oxygen} = 762 - 14.53$

$P_{oxygen} = 747.47\ mmHg = 0.98\ atm$

From

$n = \frac{PV}{RT} = n_{exp}$

Where:

V = Volume of oxygen gas collected over water at time (t) in litres (l)

$T = Laboratory\ temperature = 17\ ^{o}C = 273 + 17 = 290\ K$

$P = P_{oxygen} = 0.98\ atm$

$R = 0.0821\ l.atm.mol^{-1}.K^{-1}$

Therefore,

$$n_{exp} = \frac{PV}{RT}\frac{0.98 \times V}{0.0821 \times 290} = 0.0411609V\ mol = Amount/Moles\ of\ oxygen\ produced$$

Therefore,

$$FE\ (\%) = \frac{n_{exp}}{n_{theory}} \times 100$$

$$FE\ (\%) = \frac{0.0411609V\ mol}{0.0012435I\ mol} \times 100$$

Oxygen production rate (O_2 rate) (mol s^{-1})

$$O_2\ rate = \frac{n_{exp}}{t}$$

Where:

t = 8 mins = 480 s

$n_{exp} = 0.0411609V\ mol$

Therefore,

$$O_2\ rate = \frac{0.0411609V}{480} = 8.57519 \times 10^{-5} V\ mol\ s^{-1}$$

Table S2: Faraday's Efficiency and oxygen production rate calculations

	V vs. RHE	I (A)	V (l)	FE (%)	O_2 rate (μmol s^{-1})	O_2 produced (mmol)
NMO	1.9	0.6	0.0135	74.5	1.16	0.556
FBT	1.9	1.052	0.029	91.25	2.49	1.194
FBT/NMO(25)	1.9	1.12	0.031	91.6	2.66	1.276
FBT/NMO(50)	1.9	1.2	0.0345	95.2	2.96	1.42
FBT/NMO(75)	1.9	1.15	0.032	92.1	2.74	1.317

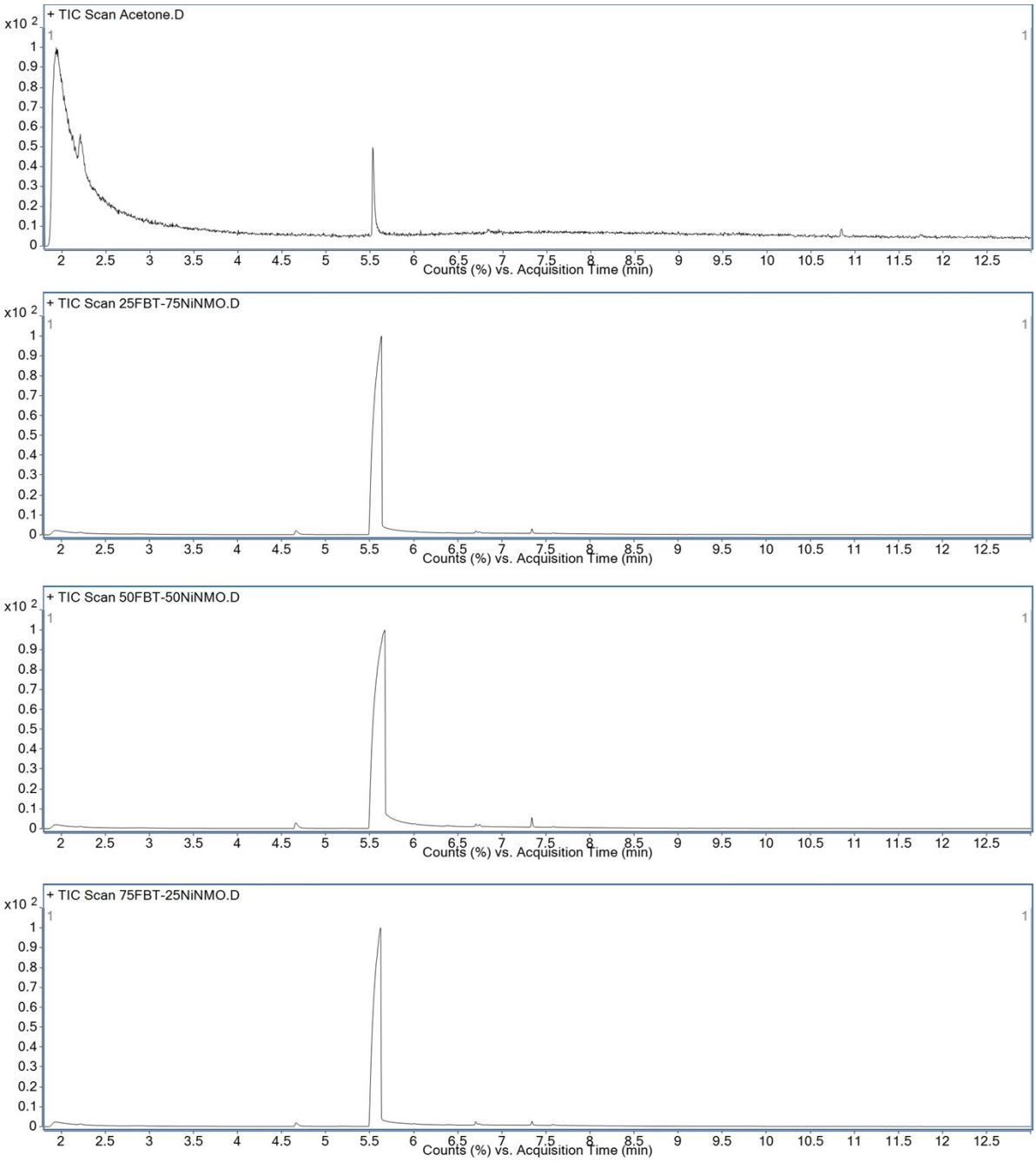

Fig. S23 Gas chromatographs of (top to bottom) acetone, FBT/NMO(25), FBT/NMO(50) and FBT/NMO(75) measured after chlorine evolution reaction (CER) test.

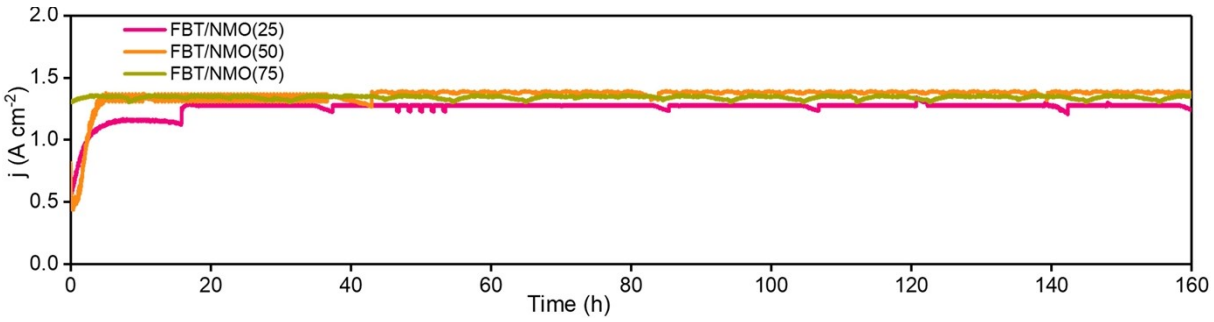

Fig. S24 Amperometric i-t Curves of FBT/NMO(25), FBT/NMO(50), and FBT/NMO(75) at 1.9 V vs RHE.

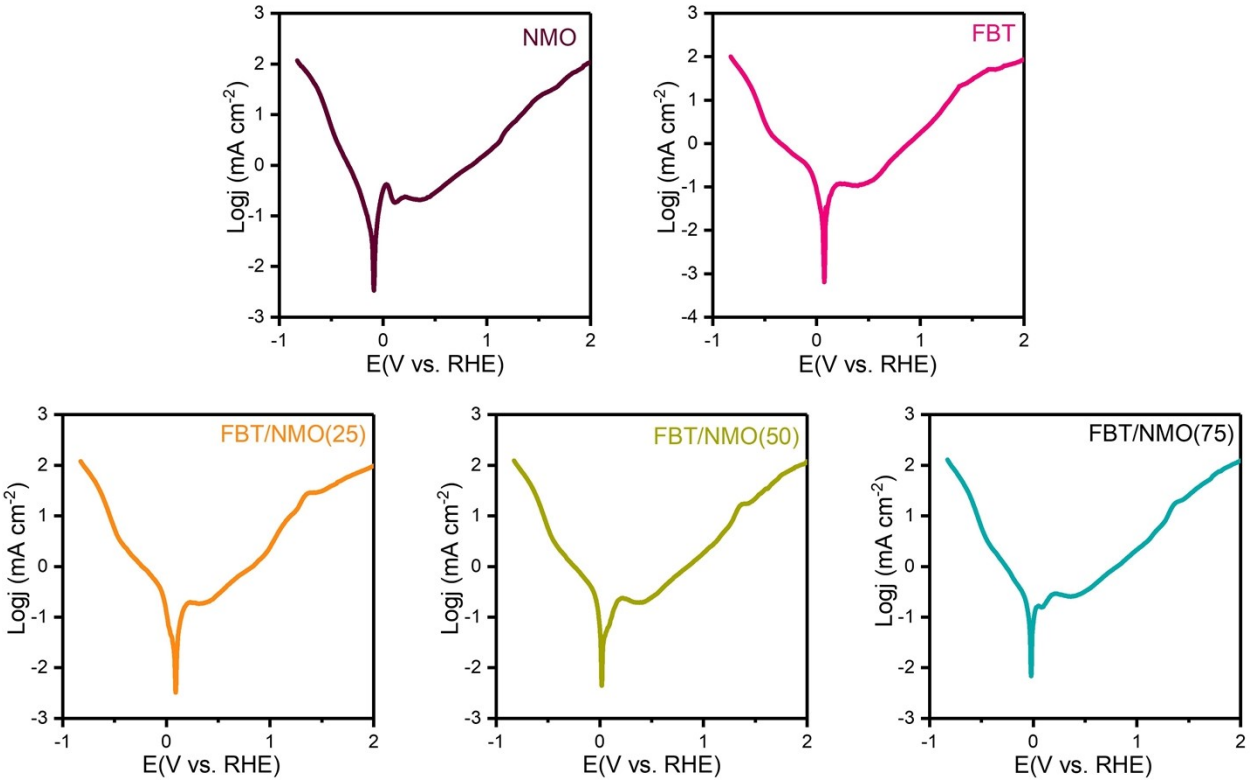

Fig. S25 Corrosion polarization curves of NMO, FBT, FBT/NMO(25), FBT/NMO(50) and FBT/NMO(75).

Table S3. Corrosion results for the synthesised catalysts.

Catalyst	E_{corr} (V vs RHE)	Logj (mA cm^{-2})	I_{corr} (mA cm^{-2})
FBT/NMO(75)	-0.02049	0.1661	1.465885
FBT/NMO(50)	0.08975	0.1975	1.575796
FBT/NMO(25)	-1.1165	0.2362	1.722662
FBT	0.07399	0.11866	1.314196
NMO	-0.08969	0.42336	2.650696

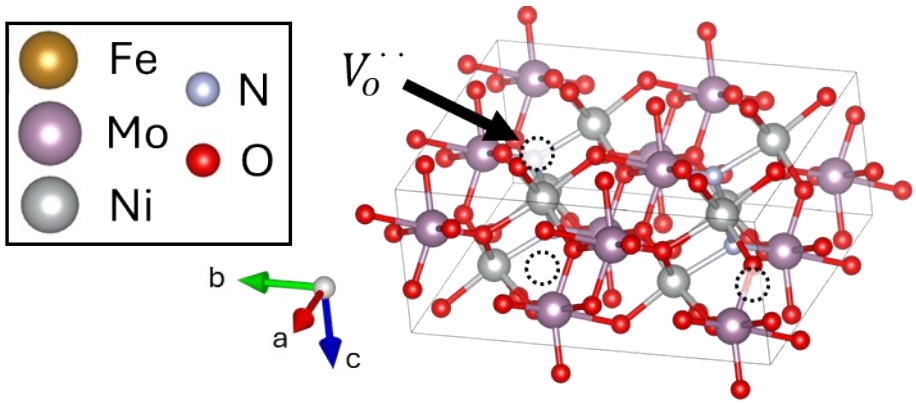

Fig. S26 Bird's-eye view of NMO($N_2Ni_7Mo_8O_{28}$) and positions of oxide ion vacancies ($V_o^{\cdot\cdot}$)

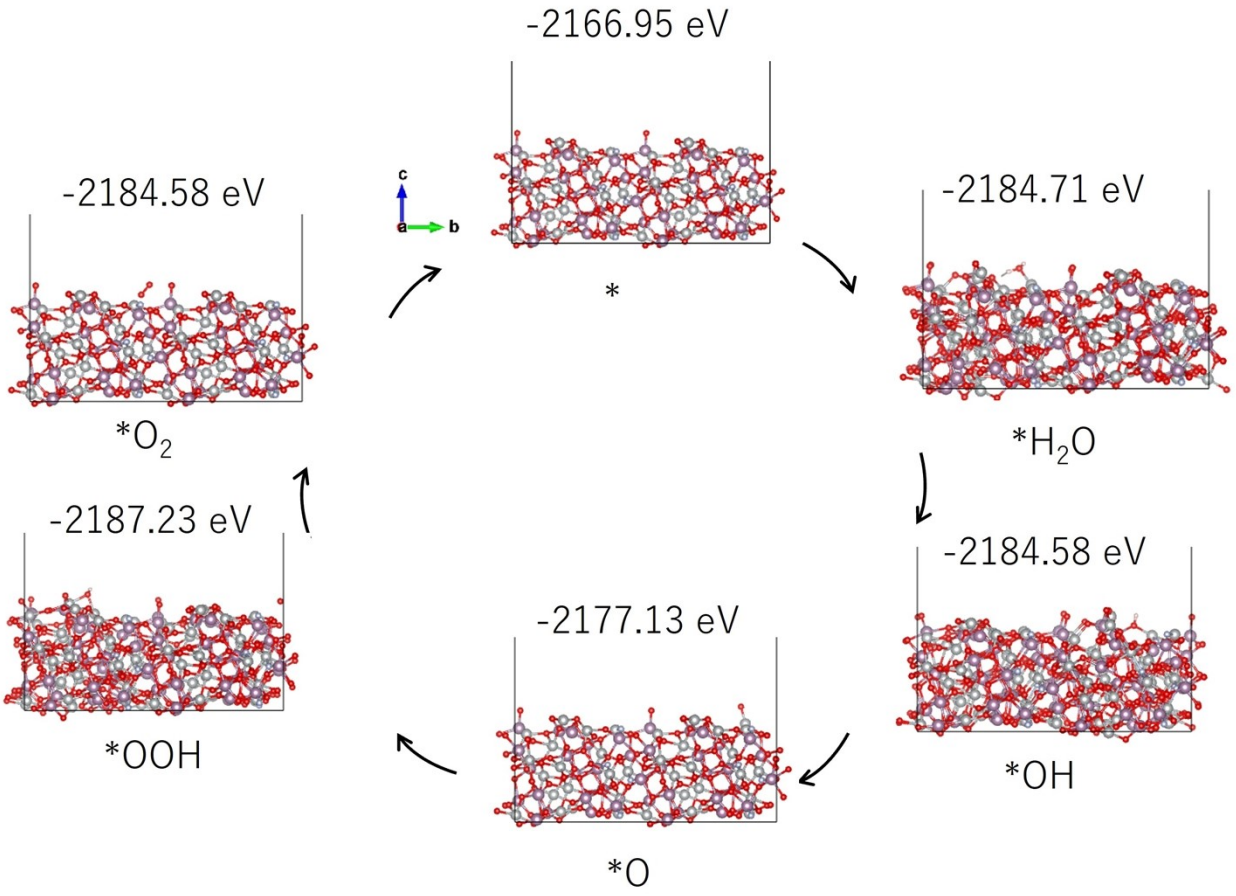

Fig. S27 Structure at each step of OER at the surface of NMO. *H_2O, *OH, *O, *OOH, *O_2, and * are molecules stabilized on the NMO.

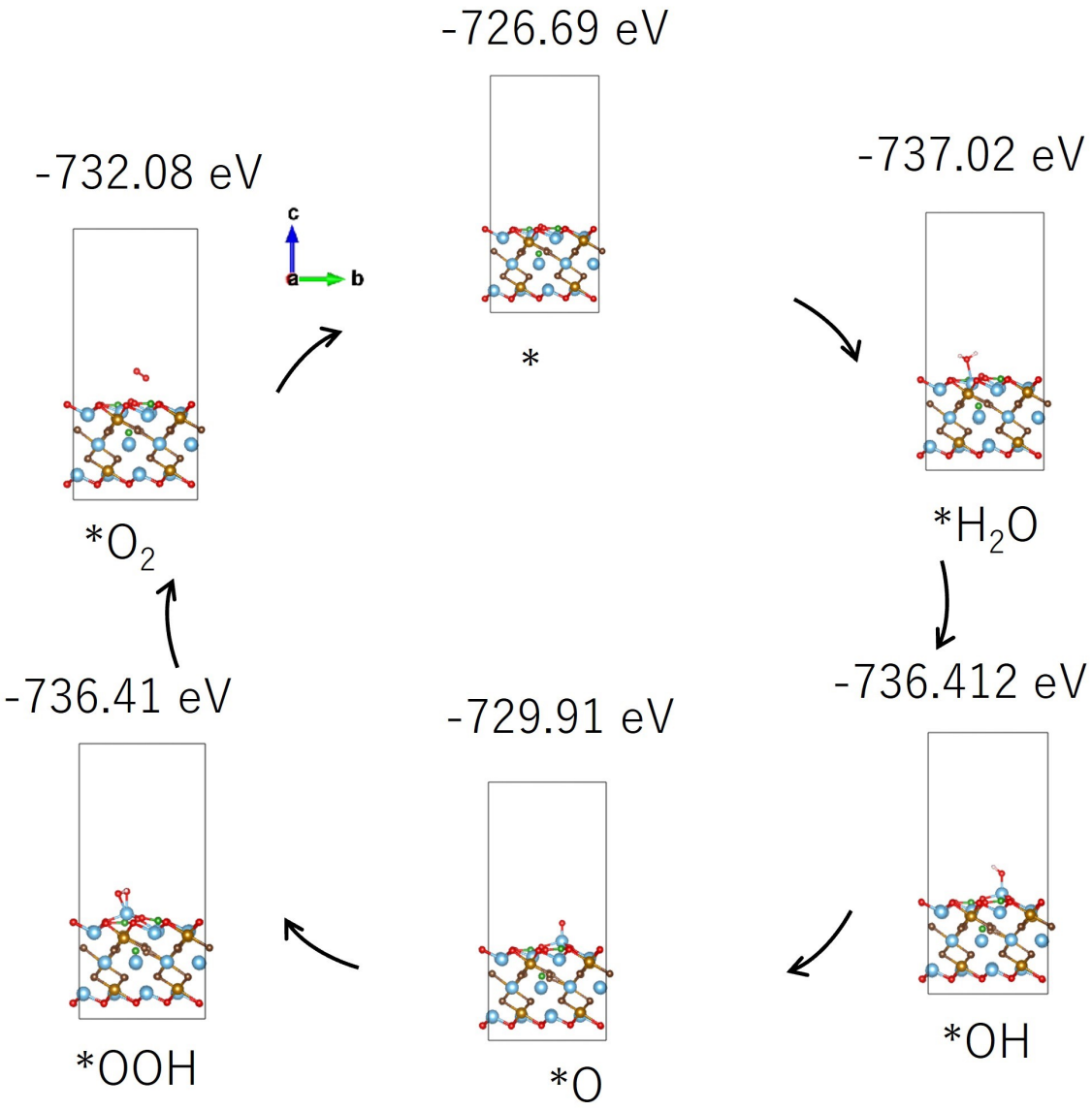

Fig. S28 Structure at each step of OER at the surface of FBT. *H_2O, *OH, *O, *OOH, *O_2, and * are molecules stabilized on the FBT.

Table S4. Total energies calculated with Matlantis for the OER intermediates (*, *H_2O, *OH, *O, *OOH) on the FBT surface, NMO surface, and FBT/NMO interface (unit = eV)

OER Intermediates	Energy (eV)		
	MNO surface	FBT surface	FBT-MNO interface
*	-2166.95	-726.69	-1934.43
*H_2O	-2184.71	-737.02	-1947.69
*OH	-2184.58	-736.41	-1945.22
*O	-2177.13	-729.91	-1941.65
*OOH	-2187.23	-736.41	-1946.83
*O_2	-2184.58	-732.08	-1942.46
E (H_2O) = -9.88 eV; E(O_2) = -5.21 eV; E(H_2) = -5.21 eV			

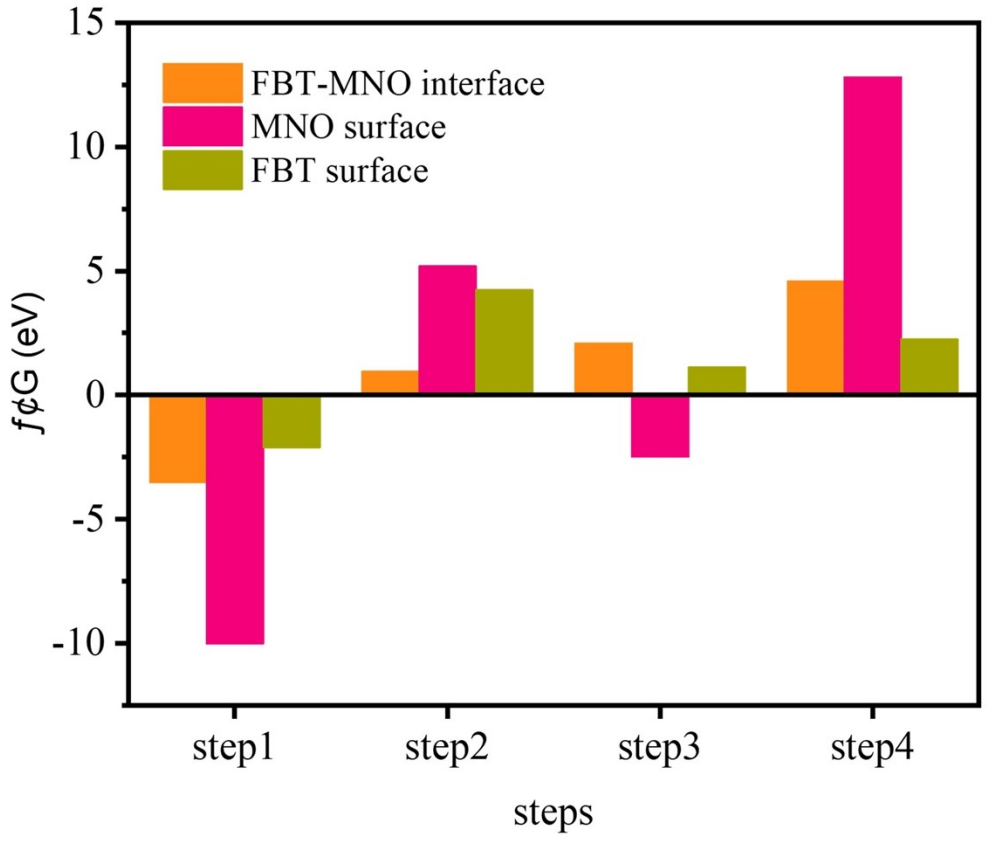

Fig. S29. Bar chart visualizing the static energies (eV) of OER intermediates on the FBT surface, NMO surface, and FBT/NMO interface as listed in Table 1. The y-axis gives Matlantis-calculated energies and the x-axis denotes the reaction of each step.

Reference

1. M. Alhabeb, K. Maleski, B. Anasori, P. Lelyukh, L. Clark, S. Sin and Y. Gogotsi, *Chem. Mater.*, 2017, **29**, 7633-7644.
2. E. Gann, C. R. McNeill, A. Tadich, B. C. C. Cowie and L. Thomsen, *J. Synchrotron Rad.*, 2016, **23**, 374-380.
3. B. C. C. Cowie, A. Tadich and L. Thomsen, *AIP Conf. Proc.*, 2010, **1234**, 307-310.
4. S. Sultan, M. Ha, D. Y. Kim, J. N. Tiwari, C. W. Myung, A. Meena, T. J. Shin, K. H. Chae and K. S. Kim, *Nat. Commun.*, 2019, **10**, 5195.
5. G. Kresse and J. Hafner, *Physical Review B*, 1993, **47**, 558-561.
6. G. Kresse and J. Furthmüller, *Physical review B*, 1996, **54**, 11169.
7. G. Kresse and D. Joubert, *Physical Review B*, 1999, **59**, 1758-1775.
8. G. Kresse and J. Furthmüller, *Computational Materials Science*, 1996, **6**, 15-50.
9. G. Kresse and J. Hafner, *Phys Rev B Condens Matter*, 1994, **49**, 14251-14269.
10. P. Sharma, M. Minakshi Sundaram, T. Watcharatharapong, S. Jungthawan and R. Ahuja, *ACS Appl Mater Interfaces*, 2021, **13**, 56116-56130.
11. W. Tang, E. Sanville and G. Henkelman, *J Phys Condens Matter*, 2009, **21**, 084204.
12. E. Sanville, S. D. Kenny, R. Smith and G. Henkelman, *J. Comput. Chem.*, 2007, **28**, 899-908.
13. G. Henkelman, A. Arnaldsson and H. Jónsson, *Computational Materials Science*, 2006, **36**, 354-360.
14. M. Yu and D. R. Trinkle, *J. Chem. Phys.*, 2011, **134**, 064111.
15. T. Fujisaki, K. Ikeda, A. T. Staykov, H. Setiawan and Y. Shiratori, *RSC Adv*, 2022, **12**, 19955-19964.
16. C. E. Calderon, J. J. Plata, C. Toher, C. Oses, O. Levy, M. Fornari, A. Natan, M. J. Mehl, G. Hart, M. Buongiorno Nardelli and S. Curtarolo, *Computational Materials Science*, 2015, **108**, 233-238.
17. T. Fujisaki, Y. Tsuji, P. H. Tu, T. C. D. Doan, D. S. Rivera Rocabado, A. T. Staykov, K. Yashiro and Y. Shiratori, *Phys. Chem. Chem. Phys.*, 2024, DOI: 10.1039/d4cp01324g.
18. T. Ichino, H. Nabata, K. Matsumoto, T. Hasegawa and S. Maeda, 2024.
19. S. Takamoto, C. Shinagawa, D. Motoki, K. Nakago, W. Li, I. Kurata, T. Watanabe, Y. Yayama, H. Iriguchi, Y. Asano, T. Onodera, T. Ishii, T. Kudo, H. Ono, R. Sawada, R. Ishitani, M. Ong, T. Yamaguchi, T. Kataoka, A. Hayashi, N. Charoenphakdee and T. Ibuka, *Nat Commun*, 2022, **13**, 2991.
20. S. Mine, T. Toyao, K.-i. Shimizu and Y. Hinuma, *Chem. Lett.*, 2023, **52**, 757-759.
21. S. Yasumura, T. Kato, Y. Qian, T. Toyao and K.-i. Shimizu, *The Journal of Physical Chemistry C*, 2024, **128**, 12949-12959.
22. H. Y. Wang, N. Q. Zhao, C. S. Shi, L. Y. Ma, F. He, C. N. He, J. J. Li and E. Z. Liu, *Electrochim. Acta*, 2017, **247**, 1030-1037.
23. L. Yu, J. Xiao, C. Huang, J. Zhou, M. Qiu, Y. Yu, Z. Ren, C.-W. Chu and J. C. Yu, *Proc. Natl. Acad. Sci.*, 2022, **119**, e2202382119.
24. C. Huang, Q. Zhou, L. Yu, D. Duan, T. Cao, S. Qiu, Z. Wang, J. Guo, Y. Xie, L. Li and Y. Yu, *Adv. Energy Mater.*, 2023, **13**, 2301475.
25. L. Teng and L. Zhao, *J. Electroanal. Chem.*, 2023, **949**, 117824.
26. X. Zhang, C. Feng, Z. Fan, B. Zhang, Y. Xiao, A. Mavrič, N. Pastukhova, M. Valant, Y.-F. Han and Y. Li, *Inorg. Chem. Front.*, 2023, **10**, 3103-3111.

27. M. Ning, F. Zhang, L. Wu, X. Xing, D. Wang, S. Song, Q. Zhou, L. Yu, J. Bao, S. Chen and Z. Ren, *Energy Environ. Sci.*, 2022, **15**, 3945-3957.
28. C. Huang, Q. Zhou, D. Duan, L. Yu, W. Zhang, Z. Wang, J. Liu, B. Peng, P. An, J. Zhang, L. Li, J. Yu and Y. Yu, *Energy Environ. Sci.*, 2022, **15**, 4647-4658.